Article

3D Imaging Millimeter Wave Circular Synthetic Aperture Radar

Renyuan Zhang and Siyang Cao *

University of Arizona, 1230 E Speedway Blvd, P.O. BOX 210104, Tucson, Arizona, 85721, USA; ryzhang@email.arizona.edu

* Correspondence: caos@email.arizona.edu; Tel.: +1-520-621-4521

Abstract: In this paper, a new millimeter wave 3D imaging radar is proposed. The user just needs to move the radar along a circular track, a high resolution 3D imaging can be generated. The proposed radar uses the movement of itself to synthesize a large aperture in both the azimuth and elevation directions. It can utilize inverse Radon transform to resolve 3D imaging. To improve the sensing result, compressed sensing approach is further investigated. The simulation and experimental result further illustrated the design. Because a single transceiver circuit is needed, a light, affordable and high resolution 3D mmWave imaging radar is illustrated in the paper.

Keywords: radar 3D imaging; synthetic aperture radar; millimeter wave radar; remote sensing; compressed sensing; inverse Radon transform; portable

1. Introduction

3D imaging radar becomes feasible in the field of remote sensing due to the advancement in solid state microwave circuits and digital signal processor [1]. However, large antenna synthesization is usually performed by airborne radar to interrogate the terrain [2], and is not suitable for civilian usage. Considering a wide usage of millimeter wave radar for automobile, security and surveillance, we are proposing a new imaging technique [3,4] combining synthetic aperture radar (SAR) and millimeter wave radar. The proposed Millimeter Wave Circular Synthetic Aperture Radar (MMWCSAR) conducts a circular trajectory to synthesize a large aperture for achieving 3D imaging. MMWCSAR has four key aspects: high-resolution, working on diversity conditions, portable and low-cost.

For high-resolution, millimeter wave radar can support hundreds megahertz for range detection. For example, automotive radar is working on millimeter wave. It can sweep hundreds of megahertz to distinguish cars and even pedestrain [5]. In addition, automotive radar has been applied on smart vehicles for 2D terrain mapping [6], collision detection, parking assistance and blind spot indicator [7]. However, the current automotive radar uses traditional strip-map SAR imaging to generate a 2D terrain mapping. The proposed MMWCSAR aims at generating 3D imaging. It can be further apply to automotive radar for better understanding of the environment.

For working on diversity conditions, we compare millimeter wave radar with optical technologies. Despite that optical imaging techniques have better resolutions due to its high center frequency, radar imaging has numerous advantages over traditional optical imaging techniques like Camera and Lidar. It is underlined in [8] that radar has superior working capacity in any weather condition, including rain, snow and fog. The complex roadway environment for automobile requires uninterrupted remote sensors performing consistantly at inclement weather. The millimeter wave radar is capable of acquiring and tracking all obstacles in its field of view (FOV) under all weather conditions [8]. MMWCSAR is an innovative imaging device capable of working on diversity conditions compared to traditional optical sensors.

For portable and low-cost features, we compare with traditional millimeter wave imaging techniques, such as, security surveillance system [9,10], concealed weapon detection [11–13] and

millimeter wave cameras [6,14]. Most of these traditional applications, including millimeter wave scanner which deploys many transceivers, are bulky and high cost system design. On the contrary, MMWCSAR adopts a monostatic radar which can minimize its size and cost. It ensures that MMWCSAR can provide a three-dimensional microwave imaging for security, indoor surveillance and automotive target detection in a wearable and inexpensive manner.

MMWCSAR requires the motion of radar in a circular track other than a straight track as traditional strip-map SAR techniques. Our study found that the movement between radar and targets produces the projections of objects to different movement directions. One can therefore obtain a Range-Projections-Angle datacube from the circular movements. From the datacube, by applying inverse Radon transform (IRT) [15,16], the datacube can be converted to FOV figure. The principles are similar to the computed tomography [15,17–20]. Jia et al. [21] presented a 2D imaging algorithm for circular SAR. The motion of the SAR is along a circular trajectory. The sub-spectrums of different angles are matched filtered and summed in Fourier domain to obtain a 2D Fourier spectrum of the imaging. By space-invariant matched filtering and 2D inverse Fourier transform (2D-IFFT), the trajectory deviation is eliminated and the final aperture view is presented. Additionally, Bao et al. [22] proposed a multi-circular SAR approach. Their multi-circular SAR samples on different elevation levels. Different circular rotation angles and down-looking angles are recorded according to the range data. Consequently, their signal processing procedure results in reconstruction of a 3D image from multi-circular SAR. In our approach, we can also use hand swinging to obtain a full-circular projections. The circular trajectory plane is parallel to the range bin plane. The range calibration is also implemented before the IRT in order to reduce the targets mismatch on the volume FOV image.

MMWCSAR tested with hand swinging is not accurate for high-resolution imaging. Additional signal processing procedure of compressed sensing (CS) can be applied in our MMWCSAR system. CS has been introduced in [23,24]. Many large data size applications behaving sparse targets have been using CS for data reduction and restoration, e.g., single-pixel imaging [25], magnetic resonance imaging (MRI) [26,27]. It has advantages on situations when sampling is expensive, slow, or difficult [28]. CS method applied in radar signal processing can sample fewer signals for the sensors while keeping the same quality of the generated imaging. With reducing size of samples for the portable radar device like MMWCSAR, a fast data acquisition can be achieved by CS method. Meanwhile, the imaging resolution can be improved.

Radar signal processing with CS is addressed in [2,21,22,29–32]. In [29], Ender gave a full analysis on applying the CS to radar pulse compression. Sevimli [30] introduced Range-Doppler compressed sensing and optimization comparison of different reconstruction algorithms. In addition to the CS used in Range-Doppler response, our method of applying CS to radar signal processing is innovative. It allows not only the Pulse-Doppler compressed sensing, but also the Slow time-Angle compressed sensing. Recent work on CS applied to SAR systems is drawing researchers' attention. For instance, Bao et al. [22] produced the 3D multi-circular SAR image using a "2D+1D" mode, i. e., 2D focused SAR images are followed by 1D profile estimation of the elevation direction. With CS applied 2D ground plane image and 1D profile of the elevation dimension, 3D figure can be reproduced. CS theory is also applicable in our MMWCSAR system. First, CS is applied to 2D Slow time-Angle data to form a 2D FOV image on a single range bin. Volume FOV figure can be reconstructed and analyzed by applying 1D range profile to 2D FOV images of different range bins. Second, to achieve the CS in radar signal processing, the sparsity and incoherence properties are discussed. In addition, 2D transformation from Slow time-Angle to Azimuth-Elevation representation matrix is discussed. Besides, we also introduce how to choose the sensing matrix, so that the CS algorithm can be realized. Finally, to further improve the performance of MMWCSAR system, we focus on decreasing the data acquisition time, improving imaging resolution and reducing errors caused by human with CS applied algorithm in experiment.

The structure of this paper is as follows. In section 2, the MMWCSAR system configuration, parameters, data acquisition, resolution and its constrains of choosing MMWCSAR system

Peer-reviewed version available at Sensors 2017, 17, , 1419; doi:10.3390/s17061419

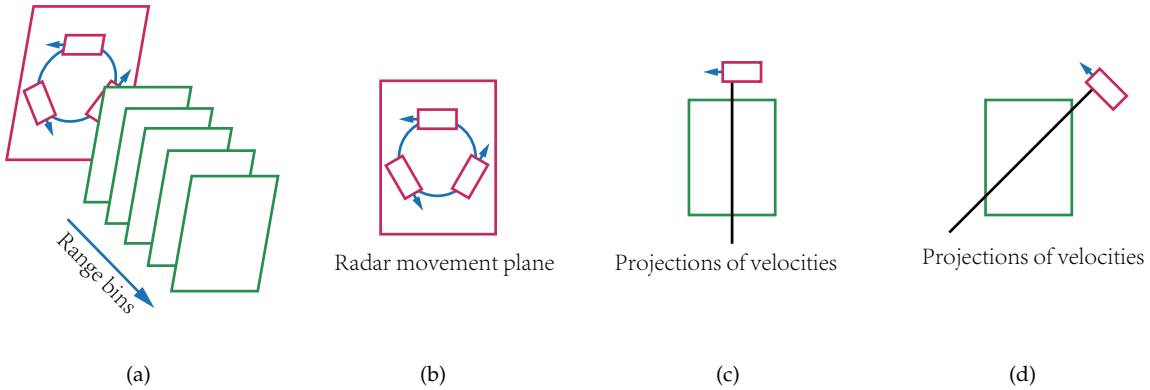

Figure 1. Uses rotation radar to resolve 3D imaging.
(a) Schematic view of resolving range using range bins.
(b) The swinging within the rotation plane of the radar generates velocities in different directions.
(c)(d) Each range bin is then projected into different velocity directions while data is collected.

parameters are introduced. In section 3, range calibration and radar imaging processing by using IRT to reconstruct the volume FOV image are presented. In section 4, we propose the CS for MMWCSAR algorithm. The corresponding simulation as well as experimental results are shown in section 5. In section 6, we discussed the results from the simulation and experiment. In section 7, we conclude the paper.

2. MMWCSAR system

The relative movement between a radar and targets can be used to detect and locate targets. Examples include SAR [2,33], inverse SAR (ISAR) [34–36], moving target indicator [7], etc. To introduce the relative movement between the proposed radar and targets, the placement of the MMWCSAR system is presented in section 2.1. The parameters for the monostatic radar is introduced in section 2.2. In 2.3, data acquisition is shown. The resolution of the MMWCSAR system is presented in section 2.4. The constrains of MMWCSAR parameters are studied in section 2.5.

2.1. MMWCSAR Configuration

The proposed 3D imaging MMWCSAR system uses a single transceiver element to acquire data from the targets by emulating multiple transceivers through movement of the single transceiver. To simplify the movement of MMWCSAR, we assume that MMWCSAR will move along a circular track. The plane of the circular track is perpendicular to the range bin axis (in Fig. 1(a)). The radar moving along the circular track keeps a constant speed, but the direction changes over time (in Fig. 1(b)).

As the radar is moving inside the plane perpendicular to the range bin axis, detected targets remain stationary within its range bin while sampling. The movement of radar produces relative speeds of detecting targets. For each separate range bin, detecting targets have different relative velocities depending on their azimuth and elevation locations. As the radar moves to different directions, the targets within a single range bin will project to different directions. If the target is at center of its range bin, the relative velocity is zero no matter the radar's movement direction. For targets away from the center, the relative velocities vary according to the radar's movement directions. Fig.1(c) and Fig. 1(d) show that targets within a range bin are projected onto different radar moving directions. Consequently, relative movement produce targets' Doppler data which can be used to distinguish targets within the same range bin.

Preprints (www.preprints.org) | NOT PEER-REVIEWED | Posted: 15 March 2017 doi:10.20944/preprints201703.0103.v1

Peer-reviewed version available at Sensors 2017, 17, , 1419; doi:10.3390/s17061419

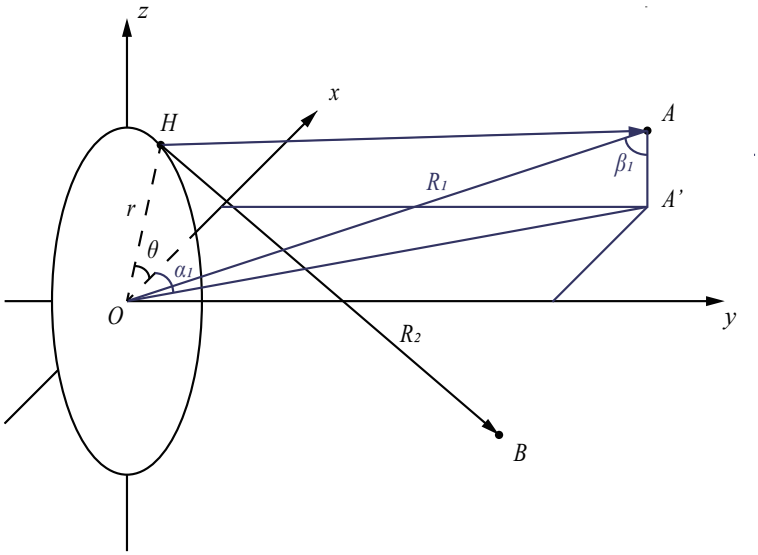

Figure 2. Geometry of monostatic radar remote sensing targets (positive y axis is the boresight direction)

As we can see from Fig. 2, the geometry of MMWCSAR is presented. H represents a monostatic radar. For different rotation positions, the Range-Azimuth-Elevation of radar can be presented in Cartesian coordinates as $(H_x, 0, H_z)$: $H_x = r\cos\theta$ and $H_z = r\sin\theta$, where r denotes the rotation radius of the MMWCSAR system, and θ is the rotation angle at which the MMWCSAR take a frame of 2D Range-Doppler data. θ is related to the angular velocity ω and acquisition time stamp t, i.e.,

$$\theta = \frac{2\pi t}{\omega}. \tag{1}$$

A, B are point targets ahead of radar with different positions and their Cartesian representation are (A_x, A_y, A_z) and (B_x, B_y, B_z). As the spherical coordinates are used for signal processing, A and B have spherical coordinates' profile of (R_1, α_1, β_1) and (R_2, α_2, β_2). The vector components of A and B relative to radar in Cartesian coordinates are

$$(A_x, A_y, A_z) = (R_1\sin\beta_1\cos\alpha_1 - r\cos\theta, R_1\sin\beta_1\sin\alpha_1, R_1\cos\beta_1 - r\sin\theta) \tag{2}$$

and

$$(B_x, B_y, B_z) = (R_2\sin\beta_2\cos\alpha_2 - r\cos\theta, R_2\sin\beta_2\sin\alpha_2, R_2\cos\beta_2 - r\sin\theta), \tag{3}$$

respectively. Equations (2) and (3) provide a method to describe targets in terms of range, azimuth angle and elevation angle instead of range, azimuth location and elevation location. The targets' 3D location profiles are independent from the radar movement as long as applying the range calibration of the displacement of the origin (radar rotation center) to the radar. The projections are projected onto each range bin and are associated with rotation angle θ. Therefore, the MMWCSAR addresses a unique approach of radar remote sensing problem.

The moving direction can be recorded by angle θ over time. The geometry of obtaining the projection angle γ can be seen from Fig. 3. Doppler velocities of the targets are the projections onto the radar rotation plane. γ can be represented using the displacement vector $\overrightarrow{HA}$ and the velocity vector $\overrightarrow{HV}$:

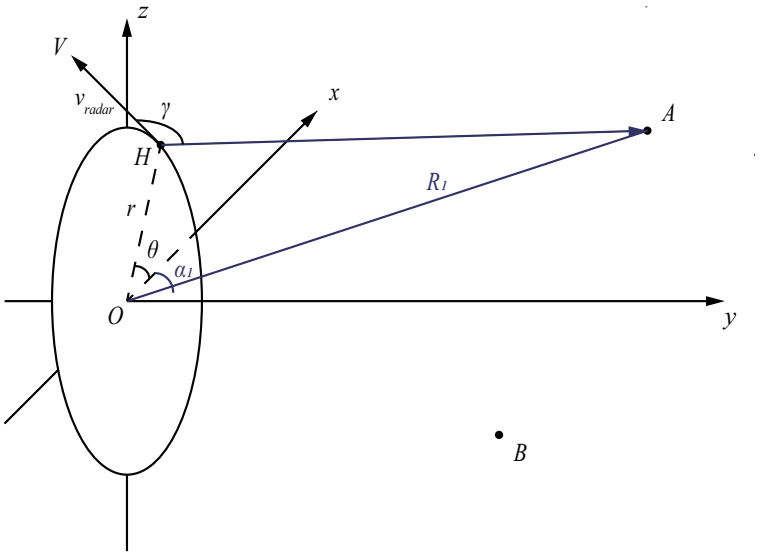

Figure 3. Geometry of monostatic radar velocity projections (positive y axis is the boresight direction)

$$\begin{aligned}\gamma &= \arccos \frac{\overrightarrow{HA} \cdot \overrightarrow{HV}}{|\overrightarrow{HA}||\overrightarrow{HV}|} \\ &= \arccos \frac{\overrightarrow{OA} \cdot \overrightarrow{HV}}{R_{revised}|v_{radar}|}\end{aligned} . \tag{4}$$

$R_{revised}$ is the revised range of the radar-target and it will be discussed in range calibration section 3.1. $|v_{radar}|$ is the magnitude of the velocity of the radar:

$$|v_{radar}| = \frac{2\pi r}{\omega} . \tag{5}$$

All vectors are derived from coordinates calculations.

2.2. MMWCSAR Parameters

As introduced above, to build a light and low-cost imaging radar, we use a monostatic radar with single transceiver element.

In our setups, the monostatic radar is transmitting linear frequency modulated (LFM) pulse waveforms and operating in Range-Doppler mode. The intermediate frequency (IF) of the radar is defined as center frequency, f_c. The bandwidth (BW) of the radar determines the range resolution. In our millimeter wave design, we use a wide bandwidth chirp. Sampling frequency, f_s, and pulse chirp duration, T_P, defines number of range bins, N_R. Pulse repetition interval (PRI) is generally characterizing the Doppler frequency, f_d, and thus limiting the swinging angular velocity, ω. The number of Doppler bins, N_D, defines the velocity resolution and curbs the scanning frames, N_{Ch}. The number of frames collected are fundamental to the final FOV image.

2.3. Data Acquisition

Radar transmission signal $s(t)$ is LFM signal. The observation of radar received signal of radar before matched filter is

$$y(t) = k \exp[j2\pi(\frac{2R}{c}\frac{(BW)}{T_P} + \frac{2vf_c}{c})t]s(t) + n(t) . \tag{6}$$

Peer-reviewed version available at Sensors 2017, 17, , 1419; doi:10.3390/s17061419

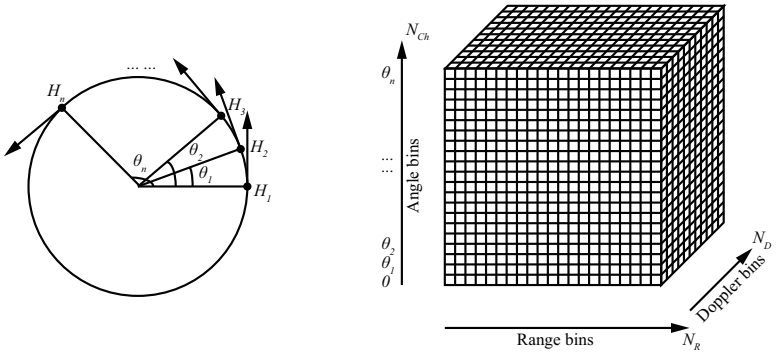

Figure 4. From projections to radar signal datacube

where k is the reflective amplitude related to the target's radar cross section (RCS), $n(t)$ is the noise, R is the range of the target. Two terms of frequency component in exponential function are fast-time and slow-time samples. These samples are frequency difference of range and Doppler, respectively.

The fast time sampling frequency of the radar determines the number of range bins, and the inter-pulses interval (i.e., slow time sampling frequency) determines the Doppler bins. Radar received signals are forming a time-series 1D signal after analog-to-digital converter (ADC). In Fig. 4, the fast-slow time samples accumulated at each angle θ_1, θ_2, ..., θ_n are reshaped by the number of range bins, N_R, and number of Doppler bins, N_D. Hence the sampling sequence of fast-time, slow-time and frames (angles) data are organized as a $N_R \times N_D \times N_{Ch}$ complex time domain data matrix. In our MMWCSAR system, the angle data recording each Range-Doppler samples is independent from Range-Doppler response. Range and Doppler samples are not overlapping as well. Consequently, the Doppler-Angle data matrix can be extracted for imaging restoration of each range bin. 3D imaging can be obtained from recovering 2D images for each range bin.

For LFM waveform, its Pulse-Doppler compression is coupled together [37]. However, in our approach, we implement compressed sensing (in section 4) to improve the final image quality of the proposed radar. The pulse compression is done separately from the Doppler compression.

After forming a 3D datacube, the uncompressed received echo signals are pulse compressed by discrete Fourier transform (DFT) of transmitted signal along range axis. In section 3, we separate the range profile and process the signal on 2D profile of the datacube to obtain the FOV figure on each range bin.

From acquisition stage, we are using the fast-time, slow-time and angles in forming a 3D datacube. The pulse compression converts the datacube into Range-Slow time-Angle datacube. And applying IRT to obtain Range-Azimuth-Elevation datacube. The last datacube is the volume FOV figure of the actual image.

2.4. MMWCSAR Resolution

The MMWCSAR system has 3D imaging capacity. So the resolution is an essential topic for high-resolution imaging.

For the range resolution, range profile is independent from the Doppler and angle profiles. Thus the range resolution is

$$\Delta R = \frac{c}{2B}. \tag{7}$$

For azimuth and elevation resolution, they are dependent on Doppler and angle profile. Both resolution are equivalent because the MMWCSAR is moving along a circular track with even angle spaces. Due to polar to Cartesian interpolation, the resolution of azimuth or elevation is higher

around the rotation center and is lower at the edge. The azimuth/elevation resolution Δl is defined as

$$\Delta l = 2l \sin \frac{\pi (PRI) N_D}{\omega}, \tag{8}$$

where l is the projection distance from center. l has limit from center of origin to the azimuth/elevation edge, which is

$$0 \leqslant l \leqslant R \tan \frac{\theta_{FOV}}{2} + r, \tag{9}$$

where θ_{FOV} denotes to the FOV angle of radar looking vision.

2.5. Constrains of Parameters

In order to reconstruct a high quality image, more data should be acquired in 3D datacube in acquisition stage. However, the number of data have some limitations as below:

2.5.1. Constrains of Number of Doppler Bins

To increase the number of angle bins, one needs to decrease the time used for capturing fast-slow time samples. As Doppler bins define the relative velocities of targets. If the target is far apart from center of its range bin, the relative velocity increases. Say, we want to have a FOV of 60° volume imaging system. We need to have enough Doppler bins to cover all the relative velocities within 60° FOV angle:

$$\frac{N_D + 1}{2} \Delta v_D \geqslant \frac{4\pi r}{\omega} \sin \frac{60^\circ}{2}, \tag{10}$$

where Δv_D is the velocity interval between two adjacent Doppler bins. Δv_D is defined as

$$\Delta v_D = \frac{c}{2 f_c (PRI)(N_D)}, \tag{11}$$

where c is the speed of electromagnetic wave.

By choosing the appropriate number of Doppler bins, the system is able to capture all needed data for Range-Doppler response within a limited given time period. Thus allows the system capture enough frames data to form a Range-Doppler-Frames datacube. In this case, the frames data serves as angle of rotation. Therefore, the 3D datacube is consisting of Range-Doppler-Angle with magnitude of the targets. The targets are assumed to be static within the sampling period. The number of Doppler bins defines the resolution on the targets' azimuth and elevation locations. The highest Doppler frequency is limited by the velocity of the radar:

$$\frac{2\pi r}{\omega} \leqslant \frac{c}{2 f_c (PRI)}. \tag{12}$$

2.5.2. Constrains of Number of Angle Bins

However, choosing too many Doppler bins results in fewer Range-Doppler responses per full-round scan. Hence the system needs to take less time in capturing per fast-slow time samples so that allows more angle data (frames data) recorded through rotating. The sampling frame time for each fast-slow time sample is:

$$T_{Ch} = (PRI)(N_D). \tag{13}$$

The radar movement is relatively constant when collecting fast-slow time samples. To achieve each sample within 10° rotation thus allowing 36 angle samples per full-round scan, we have another constrain:

$$\frac{2\pi T_{Ch}}{\omega} \leqslant 2\pi(\frac{10^\circ}{360^\circ}) . \tag{14}$$

Simplify the equation and we get:

$$\omega \geqslant 36(PRI)(N_D) . \tag{15}$$

The maximum detectable Doppler frequency is restricted by Doppler compression:

$$f_{d,\max} = \frac{2\pi r}{\omega}\frac{2f_c}{c} \leqslant \frac{2}{PRI} . \tag{16}$$

And minimum detectable Doppler frequency is restricted by Doppler compression:

$$f_{d,\min} = \frac{2\pi r}{\omega}\frac{2f_c}{c}\frac{1}{N_D} \leqslant \frac{2}{(PRI)(N_D)} . \tag{17}$$

Merging Equations (10) to (17), we get constrains with our system. A proper choice of parameters is:

$$N_D = 25,\ PRI = 30 \times 10^{-6}\ s,$$
$$r = 0.2\ m,\ \omega = 0.6\ s/round .$$

In the later sections, simulation and experiment restrictions follow constrains discussed in this section. The chosen of different parameters will result in different scanning scheme. Thus this depends on the targets. For example, we want to see the metal objects concealed behind people's clothes [38]. We need to increase the swinging rate and improve the FOV resolution. Using our constrains, we reduce our frames and PRI in order to meet the criteria.

3. Radar Imaging Processing

In this section, we discuss range calibration as well as the imaging processing for the receiving datacube.

3.1. Range Calibration

From section 2.1, additional range calibration is needed. It is because: the fan-shaped range bin should be converted into a plane-shaped range bin; the range profile of the radar should match with the rotation position as we assumed the rotation radius is zero. From Fig. 2, for a single target A, the displacement vector from radar is the actual measured range. The assumed range is from the origin, $\overrightarrow{OA} = (R_1 \sin\beta_1 \cos\alpha_1, R_1 \sin\beta_1 \sin\alpha_1, R_1 \cos\beta_1)$, which is not changing throughout time. The radar location at different time is $\overrightarrow{OH} = (r\cos(2\pi t/\omega), 0, r\sin(2\pi t/\omega))$. Thus the revised range is:

$$\begin{aligned} R_{revised} &= |\overrightarrow{HA}| = |\overrightarrow{OA} - \overrightarrow{OH}| \\ &= \sqrt{(R_1 \sin\beta_1 \cos\alpha_1 - r\cos\frac{2\pi t}{\omega})^2 + (R_1 \sin\beta_1 \sin\alpha_1)^2 + (R_1 \cos\beta_1 - r\sin\frac{2\pi t}{\omega})^2} . \end{aligned} \tag{18}$$

The range difference of the revised range and assumed range is:

$$
\begin{aligned}
R_{diff} &= R_{revised} - R = |\overrightarrow{HA}| - |\overrightarrow{OA}| \\
&= \sqrt{(R_1 \sin\beta_1 \cos\alpha_1 - r\cos\frac{2\pi t}{\omega})^2 + (R_1 \sin\beta_1 \sin\alpha_1)^2 + (R_1\cos\beta_1 - r\sin\frac{2\pi t}{\omega})^2} \\
&\quad - \sqrt{(R_1 \sin\beta_1 \cos\alpha_1)^2 + (R_1 \sin\beta_1 \sin\alpha_1)^2 + (R_1\cos\beta_1)^2}\,.
\end{aligned} \tag{19}
$$

As $|\overrightarrow{HA}|$ is only depends on the time of the rotation, thus the Range-Doppler-Angle 3D datacube can apply the calibration of range using R_{diff} at each Range-Doppler data relative to time. Time in our MMWCSAR system is related to the rotation angle θ, which is the angle profile of the datacube. A time-indexed matrix $\boldsymbol{V}$ is thus able to perform the range calibration in compressed sensing in section 4.

3.2. Radon Transform and 3D Imaging Reconstruction

Radon transform and 3D image reconstruction is illustrated in many applications, i.e., computed tomography [15] and thermoacoustic tomography [39]. Obtaining tomographic image from projections data and conversion has been introduced in [15,18–20,40,41]. The cross-sectional image of targets at each range bin is consisted of projection angle θ and the projection distance ξ. The IRT is performed for reconstruction tomography.

3.2.1. Radon Transform and Inverse Radon Transform

The Radon transform is an integral transform converts the 2D image to its projections, $p(\xi,\theta)$. The Radon transform can be defined as [15]

$$
p(\xi,\theta) = \int_{-\infty}^{\infty}\int_{-\infty}^{\infty} f(x,y)\delta(\xi - x\cos\theta - y\sin\theta)dxdy\,, \tag{20}
$$

in which $f(x,y)$ denotes to the original 2D density distribution function indexed by x and y; ξ is the projection distance from center; θ is the projection angle and $\delta(\cdot)$ is the Dirac delta function.

Its inverse transform, IRT, is widely used for image reconstructions. IRT is defined by inverting the Radon transform and therefore can reconstruct the image from the projection data. Traditionally, people used back-projection theorem to recover the inverse Radon transform [40]. Recently CT development inspired central slice theorem (CST) [15], which is the simplest method conceptually compared to back-projection and iterative algebraic techniques [20]. The theorem states that the 2D Fourier transform (FT) of the original function $f(x,y)$ is the function of 1D Fourier transforms of the projection slices in the order of angles. The 2D FT of the original function is:

$$
F(u,v) = \int_{-\infty}^{\infty}\int_{-\infty}^{\infty} f(x,y)\exp[-j2\pi(ux+vy)]dxdy\,. \tag{21}
$$

$P(\rho,\theta)$ is the 1D FT series of the projections $p(\xi,\theta)$, which can be represent by:

$$
P(\rho,\theta) = \int_{-\infty}^{\infty} p(\xi,\theta)exp(-j2\pi\rho\xi)d\xi\,. \tag{22}
$$

Hence the 2D Fourier domain function $F(u,v)$ can be obtained from the Fourier domain function $P(\rho,\theta)$ by interpolation between polar and Cartesian coordinates:

$$
P(\rho,\theta) = F(u,v)|_{u=\xi\cos\theta, v=\xi\sin\theta}\,. \tag{23}
$$

Therefore, the spatial image can be obtained from projection slices by CST. In this MMWCSAR system, the Doppler-Angle data can be converted by this algorithm to reconstruct FOV images of targets' scene at different range bins.

3.2.2. 3D Imaging Reconstruction and Range Field of View

The profile of range data is independent from the Doppler-Angle data. After the geometric calibration of the range, the Doppler-Angle can be used to reconstruction. For separate range bins, Doppler-Angle data is the projections of the final FOV figure in back-projection domain [42]. The relation is basically Radon-inverse Radon transform. Thus by using "2D+1D" model [22], range FOV 2D images are resolved at different range bins. These images are adding range bin profile to reconstruct a volume FOV figure.

4. Compressed Sensing for 3D Imaging Radar System

In terms of improving resolution and boosting the rotating accuracy, compressed sensing is used in our MMWCSAR.

4.1. Compressed Sensing Review

Basic CS idea is reviewed below. Suppose that we have a two-dimensional (2D) image with size of $A \times B$ which can be extract into a one-dimensional (1D) vector $\vec{f}$ with length of $N = AB \times 1$. Any 1D vectors can be constructed by sampling the sensing basis $\boldsymbol{\phi} = [\phi_1|\phi_2|...|\phi_M]$ [23]. M is the number of measurements of the sensing basis $\boldsymbol{\phi}$ and is smaller than the length of $\vec{f}$. Thus the sampling vector $\vec{y}$ can be expressed as:

$$\vec{y} = \phi_k \vec{f}, \quad k = 1, 2, ..., M\,. \tag{24}$$

The restriction lays the K-sparse signal $\vec{f}$ should have $K < M < N$, which allows the signal recovery from the M measurements.

CS requires the sparsity and incoherent sampling. For sparsity, we have $\vec{f} \in \mathbb{R}^N$, which is $N = AB$ pixels in the 2D image. For an orthogonal transform (DCT, wavelet transform, etc.), almost all the pixels could have sparse expansion without much perceptual loss. This results in a representation basis $\boldsymbol{\psi} = [\psi_1|\psi_2|...|\psi_N]$, which allows the following representation:

$$\vec{f} = \sum_{i=1}^{N} \psi_i x_i\,. \tag{25}$$

For incoherence sampling, from [23], the required sensing basis and representation basis should have the following incoherence parameter:

$$u(\boldsymbol{\phi}, \boldsymbol{\psi}) = \sqrt{n} \max_{1 \leqslant k,j \leqslant n} \left| \langle \phi_k, \psi_j \rangle \right|\,. \tag{26}$$

The reconstruction uses l_1-norm minimization [43–45]. The proposed solution $\hat{f}$ is constructed by $\hat{f} = \boldsymbol{\phi}\hat{x}$, where $\hat{x}$ is the solution to the convex optimization:

$$\hat{x} = \min\{\|\vec{x}\|_1 : \vec{y} = \boldsymbol{\phi}\boldsymbol{\psi}\vec{x}\}\,. \tag{27}$$

Thus the measurement $\hat{x}$ is produced by the sparsest signal of the decoding model.

4.2. Compressed Sensing on Doppler-Angle Data

As Doppler profile is in frequency domain, and angle profile is in spatial domain, slow time data is used and the pulse compression is done apart from Pulse-Doppler compression. Consequently, we have a DFT matrix of $\boldsymbol{W}$ of 1D DFT along fast-time bins, with slow-time and angle profiles repeating to match the whole 3D data size. $\boldsymbol{W^{-1}}$ is thus the transform from range frequency to fast-time samples with repetition of slow-time and angle profiles. The range calibration matrix can be expressed as $\boldsymbol{V}$.

We also implement the RT and IRT matrix for the CS. The projections on each range profile are the projections domain data of the 2D Azimuth-Elevation FOV figure. We use a rectangular IRT

Peer-reviewed version available at Sensors 2017, 17, , 1419; doi:10.3390/s17061419

matrix $\boldsymbol{U}$ transform slow-time and angle 2D data to 2D Azimuth-Elevation FOV figure with range profile repeating to match the whole 3D data size. The IRT matrix representation $\boldsymbol{U}$ is produced combined with linear interpolation from polar coordinates to Cartesian coordinates. Thus we have a conversion from the original 1D-reshaped Range-Slow time-Angle data $\vec{x}$ to the 1D-reshaped calibrated Range-Azimuth-Elevation data $\vec{b}$:

$$\vec{b} = \boldsymbol{UVW}\vec{x}\,. \tag{28}$$

Fourier transform and Radon transform are linear transforms. Both of the transformation matrices are invertable. In addition, both $\boldsymbol{U}$ and $\boldsymbol{W}$ work on 1D-reshaped Range-Slow time-Angle data. Hence CS requires solving $\vec{x}$ by using three linear mapping matrices $\boldsymbol{W^{-1}V^{-1}U^{-1}}$:

$$\vec{x} = \boldsymbol{W^{-1}V^{-1}U^{-1}}\vec{b}\,. \tag{29}$$

In this approach, the representation basis $\boldsymbol{\psi}$ is represented as:

$$\boldsymbol{\psi} = \boldsymbol{UVW}\,. \tag{30}$$

For any condensed signal $\vec{y}$, the sensing of the Range-Azimuth-Elevation data $\vec{b}$ can be expressed as:

$$\vec{y} = \boldsymbol{\phi}\vec{b}\,. \tag{31}$$

Therefore, the reconstruction is able to be implemented by using $l1$-minimization on the sensing basis $\boldsymbol{\phi}$ and the representation basis $\boldsymbol{\psi}$ from Equation (30):

$$\hat{x} = \min\{\|\vec{x}\|_1 : \vec{y} = \boldsymbol{\phi UVW}\vec{x}\}\,. \tag{32}$$

To summarize, $\boldsymbol{U}$ converts the 1D-reshaped Fast time-Slow time-Angle original data into 1D-reshaped Range-Slow time-Angle data. $\boldsymbol{V}$ is the calibration matrix of the range bins. $\boldsymbol{W}$ transforms the Range-Slow time-Angle data into 1D-reshaped Range-Azimuth-Elevation FOV figure.

4.3. Sensing Basis $\boldsymbol{\phi}$ Selection

We first define the compressed sensing ratio (CSR) as R_{CS}, expressed as:

$$R_{CS} = \frac{N}{M}\,, \tag{33}$$

M and N are numbers of rows and columns of the sensing basis, respectively. CSR is the ratio of length of the expected signal $\vec{b}$ over the length of condensed signal $\vec{y}$. It specify the reconstruction quality and size of the sensing basis and representation basis. The Slow Time-Angle data CS is done with compressing both slow time and angle. These data are transformed on each calibrated range profile. Sensing basis $\boldsymbol{\phi}$ can be expressed as follows:

1. Reduced rotation acquisition matrix
   The matrix is expressed like:

$$\phi_{k+l,k} = \begin{cases} 1, & k = 1, 2, ..., M \quad \& \quad 0 \leqslant k + l \leqslant M \\ 0, & \text{otherwise} \end{cases}. \tag{34}$$

   l is the offset depends on the rotation span. This allows sensing the expected signal with reduced rotation angles. The sensing basis reconstructs the condensed signal into a full angular projections Doppler-Angle signal along angle profile. Different projections will provide different IRT response. Thus this sensing basis enables the sampling at less angle bins which reduce

Peer-reviewed version available at Sensors 2017, 17, , 1419; doi:10.3390/s17061419

the swinging inaccuracy. This sensing matrix is also applicable on Doppler profile which also improves the projections along angle profile.

2. Reduced sampling matrix
   This matrix is expressed as:

$$\phi_{k,\lfloor R_{CS} \rfloor (k-1)+1} = \begin{cases} 1, & k = 1, 2, ..., M \\ 0, & \text{otherwise} \end{cases} . \tag{35}$$

   $\lfloor R_{CS} \rfloor$ denotes the max integer smaller than R_{CS}. This allows the sensing basis sensing the expected signal at its higher sampling rate. The sensing basis convert the condensed signal with more projections data along the Doppler or Angle bins. This method avoids swinging at inconsistent rate of the velocity. Allows the signal recovery at a better constant sinusoidal Doppler-Angle data.
3. Gaussian or random matrix
   Gaussian sensing basis is shown below:

$$\phi_k = \exp[-(k-\mu)^2/(2\sigma^2)], \quad k = 1, 2, ..., M . \tag{36}$$

   μ is the expected value of Gaussian and σ is the standard variance of Gaussian. Random is also applicable. This method allows the sampling at the normal compressed sensing procedure. This is corresponding to some CS application in MRI, i.e., [26]. The sensing basis convert the condensed signal in a smoother way. It gives the compensation to the signal. Allows the signal recovery with much more precise points along the Doppler-Angle data.

The following simulation and experiment will provide the results of CS involved MMWCSAR system. The comparison will provided with traditional IRT method.

5. Simulation and Experiment

5.1. Simulation Setup and Results

MMWCSAR is able to reconstruct the 3D image along each range bin. The following simulation provides a range of 5 meters FOV figure. The MMWCSAR system parameters can be found in Table 1. The four targets' scheme parameters are shown in Table 2.

Table 1. MMWCSAR simulation setup

Parameters	Symbol	Value
Center frequency	f_c	$76.5GHz$
Chirp starting frequency	f_{start}	$76GHz$
Chirp end frequency	f_{stop}	$77GHz$
PRI	PRI	$30 \times 10^{-}6\ s$
Chirp duration	T_P	$20 \times 10^{-}6\ s$
Fast time samples	N_R	400
Slow time samples	N_D	100
Frame samples	N_{Ch}	68
Sampling frequency	f_s	$20 \times 10^6\ Hz$
Angular velocity	ω	$0.2\ s/round$
Rotation radius	r	$0.6\ m$
Signal to noise ratio (SNR)	SNR	$10\ dB$

Peer-reviewed version available at Sensors 2017, 17, , 1419; doi:10.3390/s17061419

Table 2. Four targets' scheme setup

Parameters	Target 1	Target 2	Target 3	Target 4
Range	5 m	5 m	5 m	5 m
Azimuth location	-1.2941 m	1.7101 m	0 m	2.1131 m
Elevation location	0.8682 m	1.7101 m	0 m	-0.4358 m
RCS	1 m^2	1 m^2	1 m^2	1 m^2

As the MMWCSAR system is producing the radar transmitted LFM waveforms. The received signal together with produced Gaussian noise is analyzed with IRT method and CS involved method. The simulation results is shown in Fig. 5 with FOV figure of 5 m from the radar panel. Fig. 5(a) addresses the IRT method with perfect setup without swinging inaccuracies. The velocity of radar is changing with evenly direction and the constant magnitude. Figures 5(b) to 5(g) introduce all the CS involved method by applying different sensing basis on Slow time-Angle bins separately. For experiment, we will use Equation (34) matrix to slow time profile like in Fig. 5(d) as it provides high contrast and better resolution.

5.2. Experiment Setup and Results

With equipment from INRAS MIMO radar and three metal ball targets, a basic system can be set up. The signal processing component is a Radarbook Graphical User Interface which works at 77 GHz in Range-Doppler mode. The ball targets are metal made with high RCS which can produce high reflective beams than other targets' reflections. The parameters for experiment can be seen in Table 3. The experiment setup scheme is shown in Fig. 6(a). Ball lineup with measurement is given in Fig. 6(b). The balls are set at range of 1.21 m, 1.66 m and 2.16 m from radar panel, respectively.

Table 3. Three ball targets' scheme setup

Parameters	Target 1	Target 2	Target 3
Range	1.21 m	1.66 m	2.16 m
Azimuth angle α	$\approx -2°$	$\approx -5°$	$\approx 5°$
Elevation angle β	$\approx 0°$	$\approx 0°$	$\approx 0°$

The rotating angle per frame is around 15.3 degrees, based on calculation of 360° over number of frames N_{Ch} accumulated by the signal processing unit. Multiple swinging circles are recorded in order to reduce the impact of inaccuracies caused by hand.

The results are providing a 3D scattering plot of the FOV in front of MMWCSAR. The indices of the figure are range in meters, azimuth angle and elevation angle in degrees. The figures of applying IRT and CS methods can be seen in Fig. 7. We add the threshold to distinguish metal ball targets from the table, the board and walls.

6. Discussions

6.1. Millimeter Wave 3D Imaging Radar

For both IRT and CS method, 3D Range-Azimuth-Elevation FOV figure is recovered. The proposed system can have following advantages:

- Fast
  To recover the 3D imaging, the proposed system needs to collect data when the system is moving. A full circular movement track is needed for IRT method to collect data, while CS method can greatly decrease the number of samples. It takes only seconds for MMWCSAR to recover a FOV figure.

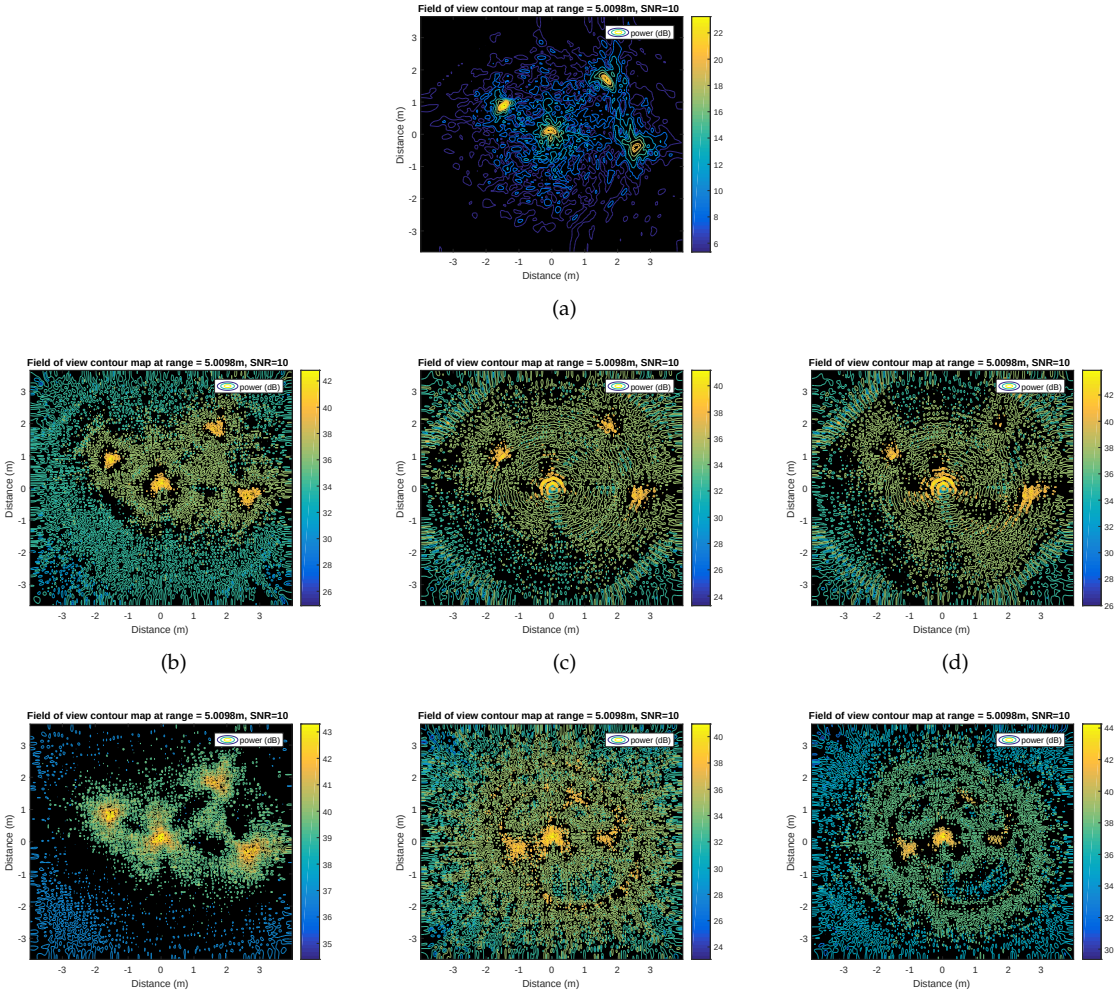

Figure 5. Simulation results

(a) IRT method with perfect setup. (b) CS applying Equation (34) to angle profile with $R_{CS} = 1/2$. (c) CS applying Equation (35) to angle profile with $R_{CS} = 1/2$. (d) CS applying Equation (36) to angle profile with $R_{CS} = 1/2$. (e) CS applying Equation (34) to slow time profile with $R_{CS} = 1/2$. (f) CS applying Equation (35) to slow time profile with $R_{CS} = 1/2$. (g) CS applying Equation (36) to slow time profile with $R_{CS} = 1/2$.

Peer-reviewed version available at Sensors 2017, 17, , 1419; doi:10.3390/s17061419

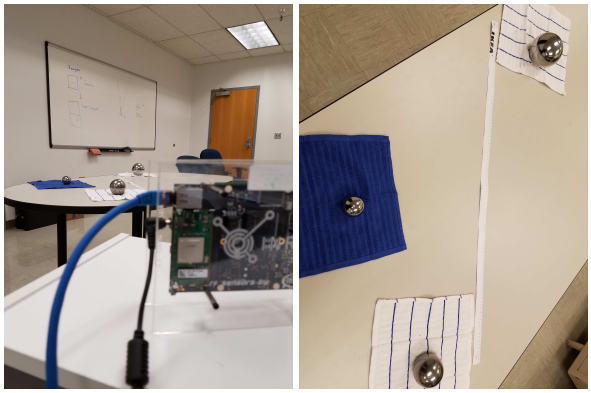

(a) (b)

Figure 6. Experiment setup
(a) Radar position with antenna facing 3 ball targets. (b) Three ball targets lineup.

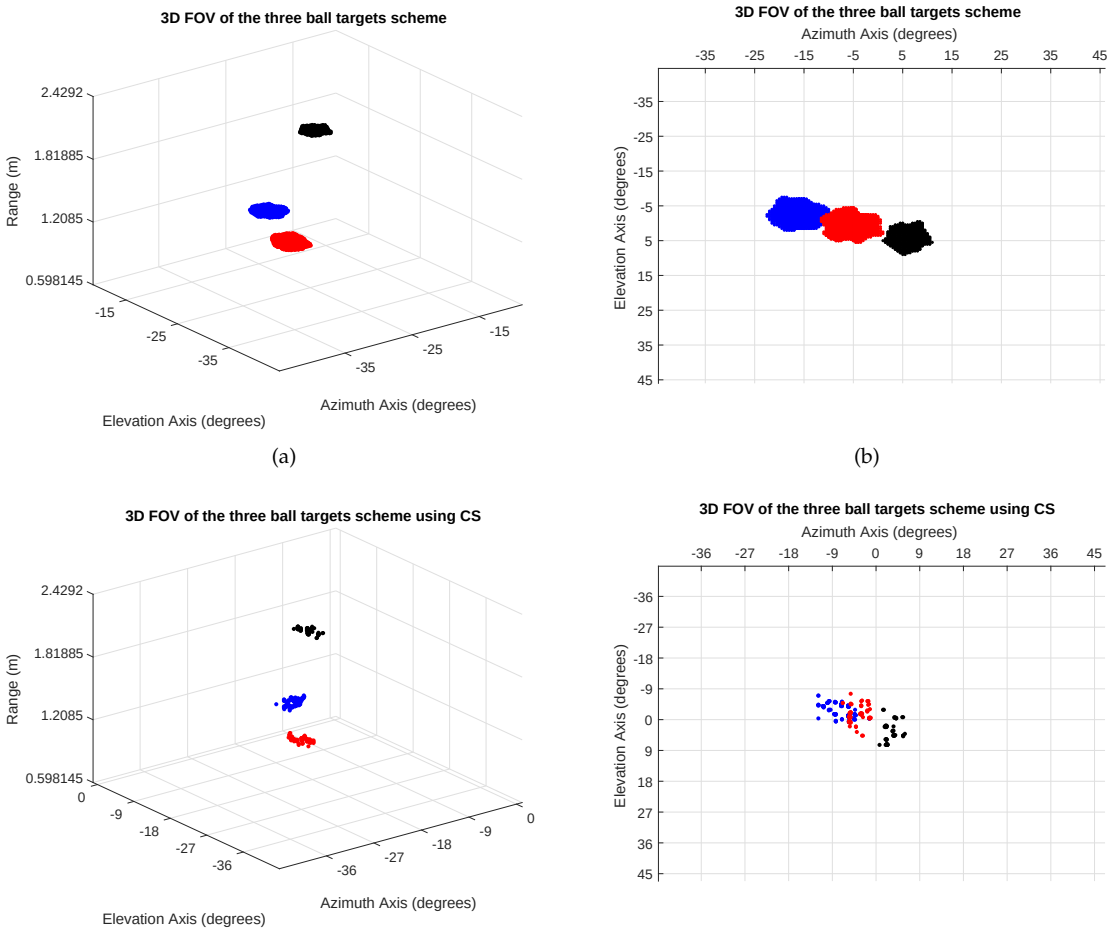

(a) (b)

(c) (d)

Figure 7. Experiment results
(a)(b) IRT method. (c)(d) CS applying Equation (34) to slow time profile.

- Portable
  Due to its size, the proposed system can be wearable for 3D imaging. Both IRT and CS method produce convincing results from simulation and experiment.
- High-resolution
  With other SAR imaging device shown in [21,22], the resolution is around 0.1 m. Our MMWCSAR working on 77 GHz can achieve 0.4 mm resolution theoretically. But by hand swinging, the resolution is reduced to around 44 mm in simulation and experiment measurements. However, it is still a high-resolution device for portable use.

6.2. Comparison with Radon Method and Compressed Sensing Method

The conversion of the 3D data matrix is linear and signal is sparse. The inverse transform of the matrix is accessible. Thus allows the CS involved method. Comparing to traditional IRT method, CS method show the following advantages:

- Flexible
  From the simulation and experiment, it is clear that the CS involved MMWCSAR system is more flexible on data reconstruction. The calculations in signal processing module is only involved of matrix multiplexing and solving $l1$-minimization. The acquisition is allowed more freedom. Based on the sampling of the targets, the CS method is able to reconstruct a better image than that of the IRT method. Data accumulated are not limited to a full circle. Mistakes and errors can be eliminated from the CS method as well. Besides, $R_{CS} = 1/2$ is used for both simulation and experiment. It is flexible to adjust the compressed sensing ratio to improve further of the MMWCSAR FOV image.
- High-SNR
  The peak of the targets are more recognizable with high decibel difference to background comparing to that of IRT method. For example, in simulation part, the CS provides 43 dB peak identification to 24 dB peak in IRT method. The peak power is measured as -32.6 dB in CS method compared to $-80.i$ dB in IRT method. Besides, improvements on FOV resolution is also noticeable. In experiment part, targets' reflective points are shown in a more accurate locations. The targets are more easily recognized by cs involved method of MMWCSAR.
- Fast-acquisition
  As matrix transformation is implemented in CS method. Huge data convolution along different axis is accomplished. Fast implementation on acquisition is achieved in the cost of more time spending on signal processing. It is a advanced signal processing method used in large data matrices in modern imaging devices.

7. Conclusions

In this paper, we present a radar system named MMWCSAR. It can generate high-resolution 3D image. The resolution and constrains of the MMWCSAR platform is discussed. We step further with the signal processing module of our system. In addition to using traditional IRT method, CS involved matrix transformation of the original data to final volume FOV image is shown.

The proposed radar system is efficient, portable and fast for widespread use. The radar transceiver used in this design is more affordable than using a MIMO imaging or traditional SAR imaging. It avoids the large antenna as well as the complex radar transceivers. A user just needs to move the radar along a circular track. A high-resolution volume FOV figure can be extracted using our algorithms.

References

1. Ahmed, S.S.; Schiessl, A.; Gumbmann, F.; Tiebout, M.; Methfessel, S.; Schmidt, L.P. Advanced microwave imaging. *IEEE microwave magazine* **2012**, *13*, 26–43.

2. Austin, C.D.; Ertin, E.; Moses, R.L. Sparse signal methods for 3-D radar imaging. *IEEE Journal of Selected Topics in Signal Processing* **2011**, *5*, 408–423.
3. Zhang, R.; Cao, S. Portable millimeter wave 3D imaging radar. (in press) 2017 IEEE Radar Conference (RadarConf17), 2017.
4. Zhang, R.; Cao, S. Compressed sensing for portable millimeter wave 3D imaging radar. (in press) 2017 IEEE Radar Conference (RadarConf17), 2017.
5. Rohling, H.; Heuel, S.; Ritter, H. Pedestrian detection procedure integrated into an 24 GHz automotive radar. 2010 IEEE Radar Conference. IEEE, 2010, pp. 1229–1232.
6. Wang, J.; Jiang, Z.; Song, Q.; Zhou, Z. Forward looking InSAR based field terrain mapping for unmanned ground vehicle. Intelligent Robot Systems (ACIRS), Asia-Pacific Conference on. IEEE, 2016, pp. 168–173.
7. Schneider, M. Automotive radar–status and trends. German microwave conference, 2005, pp. 144–147.
8. Russell, M.E.; Crain, A.; Curran, A.; Campbell, R.A.; Drubin, C.A.; Miccioli, W.F. Millimeter-wave radar sensor for automotive intelligent cruise control (ICC). *IEEE Transactions on microwave theory and techniques* **1997**, *45*, 2444–2453.
9. Cortese, F.; Flynn, T.; Francis, C.; Salloum, H.; Sedunov, A.; Sedunov, N.; Sutin, A.; Yakubovskiy, A. Experimental security surveillance system for an Island-based facility. Technologies for Homeland Security (HST), 2016 IEEE Symposium on. IEEE, 2016, pp. 1–4.
10. Appleby, R.; Anderton, R.N. Millimeter-wave and submillimeter-wave imaging for security and surveillance. *Proceedings of the IEEE* **2007**, *95*, 1683–1690.
11. Sheen, D.M.; McMakin, D.L.; Hall, T.E. Three-dimensional millimeter-wave imaging for concealed weapon detection. *IEEE Transactions on microwave theory and techniques* **2001**, *49*, 1581–1592.
12. Agarwal, S.; Kumar, B.; Singh, D. Non-invasive concealed weapon detection and identification using V band millimeter wave imaging radar system. Recent Advances in Electronics & Computer Engineering (RAECE), 2015 National Conference on. IEEE, 2015, pp. 258–262.
13. Xiao, Z.; Hu, T.; Xu, J.; Wu, L. Millimetre-wave radiometric imaging for concealed contraband detection on personnel. *IET image processing* **2011**, *5*, 375–381.
14. Yujiri, L. Passive millimeter wave imaging. 2006 IEEE MTT-S International Microwave Symposium Digest. IEEE, 2006, pp. 98–101.
15. Macovski, A. *Medical imaging systems*; Prentice Hall, 1983; pp. 113–141.
16. Lin, S.S.; Fuh, C.S. Range Data Reconstruction Using Fourier Slice Theorern. Proceedings of ICPR, 1996, Vol. 96, p. 874.
17. Miyakawa, M. Tomographic measurement of temperature change in phantoms of the human body by chirp radar-type microwave computed tomography. *Medical & biological engineering & computing* **1993**, *31*, S31–S36.
18. Kak, A.C.; Slaney, M. *Principles of computerized tomographic imaging*; IEEE press, 1988.
19. Herman, G.T. Image reconstruction from projections. *Real-Time Imaging* **1995**, *1*, 3–18.
20. Hashemi, S.; Beheshti, S.; Gill, P.R.; Paul, N.S.; Cobbold, R.S. Fast fan/parallel beam CS-based low-dose CT reconstruction. 2013 IEEE International Conference on Acoustics, Speech and Signal Processing. IEEE, 2013, pp. 1099–1103.
21. Jia, G.; Buchroithner, M.F.; Chang, W.; Liu, Z. Fourier-Based 2-D Imaging Algorithm for Circular Synthetic Aperture Radar: Analysis and Application. *IEEE Journal of Selected Topics in Applied Earth Observations and Remote Sensing* **2016**, *9*, 475–489.
22. Bao, Q.; Lin, Y.; Hong, W.; Zhang, B. Multi-circular synthetic aperture radar imaging processing procedure based on compressive sensing. Compressed Sensing Theory and its Applications to Radar, Sonar and Remote Sensing (CoSeRa), 2016 4th International Workshop on. IEEE, 2016, pp. 47–50.
23. Candès, E.J.; Wakin, M.B. An introduction to compressive sampling. *IEEE signal processing magazine* **2008**, *25*, 21–30.
24. Donoho, D.L. Compressed sensing. *IEEE Transactions on information theory* **2006**, *52*, 1289–1306.
25. Duarte, M.F.; Davenport, M.A.; Takhar, D.; Laska, J.N.; Sun, T.; Kelly, K.E.; Baraniuk, R.G.; others. Single-pixel imaging via compressive sampling. *IEEE Signal Processing Magazine* **2008**, *25*, 83.
26. Lustig, M.; Donoho, D.; Pauly, J.M. Sparse MRI: The application of compressed sensing for rapid MR imaging. *Magnetic resonance in medicine* **2007**, *58*, 1182–1195.

27. Salam, A.A.; Fawzy, F.; Shaker, N.; Kadah, Y.M. K1. High performance compressed sensing MRI image reconstruction. Radio Science Conference (NRSC), 2012 29th National. IEEE, 2012, pp. 627–631.
28. Mahalanobis, A.; Xiao, X.; Rivenson, Y.; Horisaki, R.; Stern, A.; Tanida, J.; Javidi, B. 3D Imaging with Compressive Sensing. Imaging Systems and Applications. Optical Society of America, 2013, pp. IW1E–1.
29. Ender, J.H. On compressive sensing applied to radar. *Signal Processing* **2010**, *90*, 1402–1414.
30. Sevimli, R.A.; Tofighi, M.; Cetin, A.E. Range-Doppler radar target detection using denoising within the compressive sensing framework. 2014 22nd European Signal Processing Conference (EUSIPCO). IEEE, 2014, pp. 1950–1954.
31. Herman, M.; Strohmer, T. Compressed sensing radar. 2008 IEEE Radar Conference. IEEE, 2008, pp. 1–6.
32. Yan, H.; Xu, J.; Zhang, X. Compressed sensing radar imaging of off-grid sparse targets. 2015 IEEE Radar Conference (RadarCon). IEEE, 2015, pp. 0690–0693.
33. Tian, H.; Li, D.; Li, L. Simulation of signal reconstruction based sparse flight downward-looking 3D imaging SAR. 2015 IEEE International Geoscience and Remote Sensing Symposium (IGARSS). IEEE, 2015, pp. 3762–3765.
34. Hu, X.; Tong, N.; Zhang, Y.; Wang, Y. 3D imaging using narrowband MIMO radar and ISAR technique. Wireless Communications & Signal Processing (WCSP), 2015 International Conference on. IEEE, 2015, pp. 1–5.
35. Berizzi, F.; Corsini, G. Autofocusing of inverse synthetic aperture radar images using contrast optimization. *IEEE Transactions on Aerospace and Electronic Systems* **1996**, *32*, 1185–1191.
36. Patel, V.M.; Easley, G.R.; Healy Jr, D.M.; Chellappa, R. Compressed synthetic aperture radar. *IEEE Journal of selected topics in signal processing* **2010**, *4*, 244–254.
37. Krichene, H.; Pekala, M.; Sharp, M.; Lauritzen, K.; Lucarelli, D.; Wang, I. Compressive sensing and stretch processing. 2011 IEEE RadarCon (RADAR). IEEE, 2011, pp. 362–367.
38. Blasch, E.; Ewing, R.; Liu, Z.; Pomrenke, G.; Petkie, D.; Reinhardt, K. Image fusion of the terahertz-visual naecon grand challenge data. Aerospace and Electronics Conference (NAECON), 2012 IEEE National. IEEE, 2012, pp. 220–227.
39. Haltmeier, M.; Scherzer, O.; Burgholzer, P.; Nuster, R.; Paltauf, G. Thermoacoustic tomography and the circular Radon transform: exact inversion formula. *Mathematical Models and Methods in Applied Sciences* **2007**, *17*, 635–655.
40. Xu, M.; Wang, L.V. Universal back-projection algorithm for photoacoustic computed tomography. *Physical Review E* **2005**, *71*, 016706.
41. Stergiopoulos, S. *Advanced signal processing handbook: theory and implementation for radar, sonar, and medical imaging real time systems*; CRC press, 2000.
42. Duersch, M.I. Backprojection for synthetic aperture radar. PhD thesis, Brigham Young University-Provo, 2013.
43. Candes, E.; Romberg, J. l1-magic: Recovery of sparse signals via convex programming. *URL: www. acm. caltech. edu/l1magic/downloads/l1magic. pdf* **2005**, *4*, 14.
44. Romberg, J. Imaging via compressive sampling [introduction to compressive sampling and recovery via convex programming]. *IEEE Signal Processing Magazine* **2008**, *25*, 14–20.
45. Zhang, Y. Theory of Compressive Sensing via l1-Minimization: a Non-RIP Analysis and Extensions. *Journal of the Operations Research Society of China* **2013**, *1*, 79–105.